Frequency-velocity-scalar filtered mass density function for large eddy simulation of turbulent flows

M. R. H. Sheikhi,[1,a)] P. Givi,[1] and S. B. Pope[2]
[1]*Department of Mechanical Engineering and Materials Science, University of Pittsburgh, Pittsburgh, Pennsylvania 15261, USA*
[2]*Sibley School of Mechanical and Aerospace Engineering, Cornell University, Ithaca, New York 14853, USA*

(Received 14 November 2008; accepted 2 May 2009; published online 15 July 2009)

A methodology termed "frequency-velocity-scalar filtered mass density function" (FVS-FMDF) is developed for large eddy simulation (LES) of turbulent flows. The FVS-FMDF takes account of unresolved subgrid scales (SGSs) by considering the joint probability density function (PDF) of the frequency, the velocity, and the scalar fields. An exact transport equation is derived for the FVS-FMDF in which the effects of convection and chemical reaction are in closed forms. The unclosed terms in this equation are modeled in a fashion similar to PDF methods in Reynolds-averaged Navier–Stokes simulations. The FVS-FMDF transport is modeled via a set of stochastic differential equations (SDEs). The numerical solution procedure is based on a hybrid finite-difference (FD)/Monte Carlo (MC) method in which the LES filtered transport equations are solved by the FD, and the set of SDEs is solved by a Lagrangian MC procedure. LES of a temporally developing mixing layer is conducted via the FVS-FMDF, and the results are compared with those via the Smagorinsky SGS closure. All these results are also assessed by comparison with those obtained by direct numerical simulation (DNS). The FVS-FMDF predictions show favorable agreements with DNS data. © *2009 American Institute of Physics*. [DOI: 10.1063/1.3153907]

I. INTRODUCTION

The objective of large eddy simulation (LES) is to resolve the turbulent unsteady large scale motions directly while accounting for the small scale motions via a subgrid scale (SGS) model. In LES of turbulent reactive flows, this is particularly challenging due to the complex nature of turbulence-chemistry interactions. The filtered density function (FDF) (Refs. 1 and 2) has proven quite effective in this regard, as it accounts for the effects of chemical reaction in a closed form. The fundamental property of FDF is to take account of SGS effects in a probabilistic manner. There have been significant recent contributions on application of FDF to various flame configurations,[3–7] all of which are based on the scalar FDF (SFDF).[8,9] In this approach, the FDF of scalar variables are considered; therefore, a SGS closure, similar to "conventional" LES, is needed. With the development of the velocity FDF (VFDF),[10] the model was extended for SGS closure of the hydrodynamics. In VFDF the effect of SGS convection appears in a closed form. Nevertheless, the VFDF is only suitable for constant-density nonreacting flows since it contains no information on the scalar fields. This is circumvented by considering the joint velocity-scalar FDF (VSFDF) for constant-density flows[11] and the joint velocity-scalar filtered mass density function (VSFMDF) for variable-density flows.[12]

The FDF is shown to describe the complex turbulent transport more accurately compared to conventional SGS models,[10–12] as it contains the complete information on joint SGS statistics of the velocity and the scalar fields. However, due to its lack of information on flow scales, the SGS time scale is obtained from additional *ad hoc* models. The objective of the present work is to provide a "complete" closure for LES by embedding the information about the scales within the framework of FDF. This is achieved by extending the definition of FDF to include the frequency and defining the "frequency-velocity-scalar filtered mass density function" (FVS-FMDF). This approach is similar to that used in Reynolds-averaged Navier–Stokes (RANS)/probability density function (PDF),[1,13–16] in which stochastic frequency models are developed to represent the statistical behavior of the instantaneous dissipation. A differential frequency model is constructed here to allow the frequency to relax to a filtered frequency model widely used in conventional LES. The SGS mixing frequency is based on the conditional frequency model[1,14,15] which represents the filtered value of the particles. This treatment results in smaller numerical fluctuations in stochastic variables. The FVS-FMDF provides a more realistic representation of the stochastic particles by taking account of their history and origin.[17,18] The complete information on joint velocity-scalar-frequency statistics provided by this methodology is useful for a more realistic modeling of complex turbulent reactive flows.

With the modeled FVS-FMDF, LES is conducted of a three-dimensional (3D) temporally developing mixing layer. The simulated results are compared with those predicted by the Smagorinsky[19] SGS closure. All these results are assessed by comparison with direct numerical simulation (DNS) of the same layer.

[a)]Author to whom correspondence should be addressed. Telephone: 412-624-9755. Fax: 412-624-4846. Electronic mail: moh3@pitt.edu.

II. FORMULATION

In a low Mach number turbulent reactive flow, the compressible form of conservation equations, the continuity, the Navier–Stokes, the energy (enthalpy), and the scalar transport,[20]

$$\frac{\partial \rho}{\partial t} + \frac{\partial \rho u_j}{\partial x_j} = 0, \tag{1a}$$

$$\frac{\partial \rho u_i}{\partial t} + \frac{\partial \rho u_j u_i}{\partial x_j} = -\frac{\partial p}{\partial x_i} + \frac{\partial \tau_{ji}}{\partial x_j}, \tag{1b}$$

$$\frac{\partial \rho \phi_\alpha}{\partial t} + \frac{\partial \rho u_j \phi_\alpha}{\partial x_j} = -\frac{\partial J_j^\alpha}{\partial x_j} + \rho S_\alpha, \quad \alpha = 1,2,\ldots, \quad \sigma = N_s + 1, \tag{1c}$$

govern the space ($\mathbf{x} \equiv x_i$, $i=1,2,3$) and time (t) variations of the fluid density $\rho(\mathbf{x},t)$, the velocity vector $\boldsymbol{u} \equiv u_i(\mathbf{x},t)$, the pressure $p(\mathbf{x},t)$, and the compositional scalars $\phi_\alpha(\mathbf{x},t)$. Compositional scalars ϕ_α ($\alpha=1,\ldots,N_s+1$) represent the mass fraction of N_s chemical species and enthalpy. These equations, along with an equation of state,

$$p = \rho R^0 T \sum_{\alpha=1}^{N_s} Y_\alpha / M_\alpha = \rho R T, \tag{2}$$

form a closed set of equations. In Eq. (2), R^0 and R are the universal and mixture gas constants and M_α denotes the molecular weight of species α. The chemical reaction source terms $S_\alpha \equiv \hat{S}_\alpha[\boldsymbol{\phi}(\mathbf{x},t)]$ are functions of compositional scalars ($\boldsymbol{\phi} \equiv [\phi_1, \phi_2, \ldots, \phi_{N_s+1}]$). For a Newtonian fluid, with Fick's law of diffusion, the viscous stress tensor τ_{ij} and the scalar flux J_j^α are represented by

$$\tau_{ij} = \mu\left(\frac{\partial u_i}{\partial x_j} + \frac{\partial u_j}{\partial x_i} - \frac{2}{3}\frac{\partial u_k}{\partial x_k}\delta_{ij}\right), \quad J_j^\alpha = -\gamma \frac{\partial \phi_\alpha}{\partial x_j}, \tag{3}$$

where μ is the fluid dynamic viscosity and $\gamma = \rho\Gamma$ denotes the thermal and mass molecular diffusivity coefficients for all the scalars. We assume unity Schmidt and Prandtl numbers. Here for simplicity, the viscosity and molecular diffusivity coefficients are assumed to be constants.

In LES, the transport equations are filtered using the spatial filtering operation[1,21–24]

$$\langle f(\mathbf{x},t)\rangle_\ell = \int_{-\infty}^{+\infty} f(\mathbf{x}',t) G(\mathbf{x}',\mathbf{x}) d\mathbf{x}', \tag{4}$$

where $G(\mathbf{x}',\mathbf{x})$ represents the filter function with characteristic width Δ. We consider a filter function that is spatially and temporally invariant and localized; thus, $G(\mathbf{x}',\mathbf{x}) \equiv G(\mathbf{x}'-\mathbf{x})$ with the properties $G(\mathbf{x}) \geq 0$ and $\int_{-\infty}^{+\infty} G(\mathbf{x}) d\mathbf{x} = 1$. The filtered and Favre filtered values of variable $f(\mathbf{x},t)$ are denoted by $\langle f(\mathbf{x},t)\rangle_\ell$ and $\langle f(\mathbf{x},t)\rangle_L = \langle \rho f\rangle_\ell / \langle \rho\rangle_\ell$, respectively. The filtered form of the governing equations [Eqs. (1a)–(1c)] are

$$\frac{\partial \langle \rho\rangle_\ell}{\partial t} + \frac{\partial \langle \rho\rangle_\ell \langle u_i\rangle_L}{\partial x_i} = 0, \tag{5a}$$

$$\frac{\partial \langle \rho\rangle_\ell \langle u_i\rangle_L}{\partial t} + \frac{\partial \langle \rho\rangle_\ell \langle u_i\rangle_L \langle u_j\rangle_L}{\partial x_j} = -\frac{\partial \langle p\rangle_\ell}{\partial x_i} + \frac{\partial \langle \tau_{ij}\rangle_\ell}{\partial x_j} - \frac{\partial \langle \rho\rangle_\ell \tau(u_i,u_j)}{\partial x_j}, \tag{5b}$$

$$\frac{\partial \langle \rho\rangle_\ell \langle \phi_\alpha\rangle_L}{\partial t} + \frac{\partial \langle \rho\rangle_\ell \langle u_i\rangle_L \langle \phi_\alpha\rangle_L}{\partial x_i} = -\frac{\partial \langle J_i^\alpha\rangle_\ell}{\partial x_i} - \frac{\partial \langle \rho\rangle_\ell \tau(u_i,\phi)}{\partial x_i} + \langle \rho\rangle_\ell \langle S_\alpha\rangle_L. \tag{5c}$$

The closure problem is associated with the SGS stress $\tau(u_i,u_j)$, the SGS scalar flux $\tau(u_i,\phi)$, and the filtered chemical reaction source term $\langle S_\alpha\rangle_L$, where $\tau(a,b) = \langle ab\rangle_L - \langle a\rangle_L \langle b\rangle_L$.

III. THE FREQUENCY-VELOCITY-SCALAR FILTERED MASS DENSITY FUNCTION

A. Definitions

For the scalar array $\boldsymbol{\phi}(\mathbf{x},t)$ ($\boldsymbol{\phi} \equiv [\phi_1, \phi_2, \ldots, \phi_{N_s+1}]$), the velocity $\boldsymbol{u}(\mathbf{x},t)$, and the frequency $\omega(\mathbf{x},t)$ (Ref. 16) fields, the complete SGS statistical information is included in the FVS-FMDF which is formally defined as[1,12]

$$P_L(\theta,\boldsymbol{v},\boldsymbol{\psi},\mathbf{x};t) = \int_{-\infty}^{+\infty} \rho(\mathbf{x}',t)\zeta[\theta,\boldsymbol{v},\boldsymbol{\psi};\omega(\mathbf{x}',t),\boldsymbol{u}(\mathbf{x}',t),\boldsymbol{\phi}(\mathbf{x}',t)] G(\mathbf{x}'-\mathbf{x}) d\mathbf{x}', \tag{6}$$

where

$$\zeta[\theta,\boldsymbol{v},\boldsymbol{\psi};\omega(\mathbf{x},t),\boldsymbol{u}(\mathbf{x},t),\boldsymbol{\phi}(\mathbf{x},t)] \equiv \delta[\theta-\omega(\mathbf{x},t)] \prod_{i=1}^{3} \delta[v_i - u_i(\mathbf{x},t)] \prod_{\alpha=1}^{N_s+1} \delta[\psi_\alpha - \phi_\alpha(\mathbf{x},t)], \tag{7}$$

is the "fine-grained" density[25,26] and δ denotes the Dirac delta function. In this equation, θ, $\boldsymbol{v}$, and $\boldsymbol{\psi}$ are the sample space variables corresponding to frequency, velocity vector, and scalar array, respectively. The FVS-FMDF is the spatially filtered value of the fine-grained density and has all the properties of a mass density function.[26] For further developments it is useful to define the "conditional filtered value" of the variable $Q(\mathbf{x},t)$ as

$$\langle Q|\theta,\boldsymbol{v},\boldsymbol{\psi}\rangle_\ell = \langle Q(\mathbf{x},t)|\omega(\mathbf{x},t)=\theta,\boldsymbol{u}(\mathbf{x},t)=\boldsymbol{v},\boldsymbol{\phi}(\mathbf{x},t)=\boldsymbol{\psi}\rangle_\ell \equiv \frac{\int_{-\infty}^{+\infty} Q(\mathbf{x}',t)\rho(\mathbf{x}',t)\zeta[\theta,\boldsymbol{v},\boldsymbol{\psi};\omega(\mathbf{x}',t),\boldsymbol{u}(\mathbf{x}',t),\boldsymbol{\phi}(\mathbf{x}',t)]G(\mathbf{x}'-\mathbf{x})d\mathbf{x}'}{P_L(\theta,\boldsymbol{v},\boldsymbol{\psi},\mathbf{x};t)}. \tag{8}$$

The filtered value of any function of the frequency, velocity, and/or scalar variables $\hat{Q}(\theta,\boldsymbol{v},\boldsymbol{\psi})$ is obtained by integration over the frequency, velocity, and scalar sample space,

$$\langle\rho(\mathbf{x},t)\rangle_\ell\langle Q(\mathbf{x},t)\rangle_L = \int\int\cdots\int_{-\infty}^{+\infty}\hat{Q}(\theta,\boldsymbol{v},\boldsymbol{\psi})P_L(\theta,\boldsymbol{v},\boldsymbol{\psi},\mathbf{x};t)d\theta d\boldsymbol{v}d\boldsymbol{\psi}. \tag{9}$$

B. Exact FVS-FMDF transport equation

The time derivative of the fine-grained density function, Eq. (7), is obtained from

$$\frac{\partial\zeta}{\partial t} = -\left(\frac{\partial u_i}{\partial t}\frac{\partial\zeta}{\partial v_i} + \frac{\partial\phi_\alpha}{\partial t}\frac{\partial\zeta}{\partial\psi_\alpha} + \frac{\partial\omega}{\partial t}\frac{\partial\zeta}{\partial\theta}\right). \tag{10}$$

By substituting for velocity and scalar time derivatives from Eqs. (1a)–(1c) in this equation and performing the filtering operation, according to Eq. (6), an exact transport equation for the FVS-FMDF is obtained as[12]

$$\begin{aligned}\frac{\partial P_L}{\partial t} + \frac{\partial v_i P_L}{\partial x_i} = &-\frac{\partial}{\partial\psi_\alpha}(S_\alpha(\boldsymbol{\psi})P_L) \\ &+\frac{\partial}{\partial v_i}\left[\left\langle\frac{1}{\rho(\boldsymbol{\phi})}\frac{\partial p}{\partial x_i}|\theta,\boldsymbol{v},\boldsymbol{\psi}\right\rangle_\ell P_L\right] \\ &-\frac{\partial}{\partial v_i}\left[\left\langle\frac{1}{\rho(\boldsymbol{\phi})}\frac{\partial\tau_{ij}}{\partial x_j}|\theta,\boldsymbol{v},\boldsymbol{\psi}\right\rangle_\ell P_L\right] \\ &+\frac{\partial}{\partial\psi_\alpha}\left[\left\langle\frac{1}{\rho(\boldsymbol{\phi})}\frac{\partial J_i^\alpha}{\partial x_i}|\theta,\boldsymbol{v},\boldsymbol{\psi}\right\rangle_\ell P_L\right] \\ &-\frac{\partial}{\partial\theta}\left(\left\langle\frac{D\omega}{Dt}|\theta,\mathbf{v},\boldsymbol{\psi}\right\rangle_\ell P_L\right),\end{aligned} \tag{11}$$

where $D\omega/Dt=\partial\omega/\partial t+u_i(\partial\omega/\partial x_i)$. In this equation, the effects of convection, the second term on left-hand side, and chemical reaction, the first term on the right-hand side, appear in closed forms. The conditional filter terms represent convective effects in the frequency-velocity-scalar sample space and are unclosed.

C. Modeled FVS-FMDF transport equation

The transport of FVS-FMDF is modeled by a "stochastic particle system" governed by a set of stochastic differential equations (SDEs),[1,12]

$$dX_i^+ = U_i^+dt + \sqrt{\frac{2\mu}{\langle\rho\rangle_\ell}}dW_i, \tag{12a}$$

$$\begin{aligned}dU_i^+ = &\left[-\frac{1}{\langle\rho\rangle_\ell}\frac{\partial\langle p\rangle_\ell}{\partial x_i} + \frac{2}{\langle\rho\rangle_\ell}\frac{\partial}{\partial x_j}\left(\mu\frac{\partial\langle u_i\rangle_L}{\partial x_j}\right)\right. \\ &\left.+\frac{1}{\langle\rho\rangle_\ell}\frac{\partial}{\partial x_j}\left(\mu\frac{\partial\langle u_j\rangle_L}{\partial x_i}\right) - \frac{2}{3}\frac{1}{\langle\rho\rangle_\ell}\frac{\partial}{\partial x_i}\left(\mu\frac{\partial\langle u_j\rangle_L}{\partial x_j}\right)\right]dt \\ &+G_{ij}(U_j^+ - \langle u_j\rangle_L)dt + \sqrt{C_0k\Omega}dW_i' \\ &+\sqrt{\frac{2\mu}{\langle\rho\rangle_\ell}}\frac{\partial\langle u_i\rangle_L}{\partial x_j}dW_j,\end{aligned} \tag{12b}$$

$$d\phi_\alpha^+ = -C_\phi\Omega(\phi_\alpha^+ - \langle\phi_\alpha\rangle_L)dt + S_\alpha(\boldsymbol{\phi}^+)dt, \tag{12c}$$

$$d\omega^+ = -C_\omega\Omega(\omega^+ - \hat{\omega})dt. \tag{12d}$$

These SDEs are diffusion processes[27] with $X_i^+(t)$, $U_i^+(t)$, $\phi_\alpha^+(t)$, and $\omega^+(t)$ representing stochastic processes corresponding to position, velocity, scalar variables, and frequency, respectively. The W terms denote the Wiener–Lévy processes.[27] The terms $k=\tau(u_i,u_i)/2$ and Ω denote the SGS kinetic energy and the SGS mixing frequency, respectively. In this equation, the simplified Langevin model (SLM)[18,28–30] is employed combined with the linear mean square estimation,[31] also known as interchange by exchange with the mean[32] closure. In SLM, the term G_{ij} is modeled as

$$G_{ij} = -\Omega\left(\tfrac{1}{2}+\tfrac{3}{4}C_0\right)\delta_{ij}, \tag{13}$$

which corresponds to Rotta's model in RANS.[30] The effect of model constants C_0 and C_ϕ has been studied extensively in our previous works.[10,11] The values $C_0=2.1$ and $C_\phi=1$ are chosen as suggested in the literature.[30] The SGS mixing frequency Ω is defined as the conditional filtered frequency

$$\Omega \equiv C_\Omega\langle\omega^+|\omega^+\geq\langle\omega\rangle_L\rangle_L, \tag{14}$$

similar to that in RANS/PDF.[1,14,15] The C_Ω value is determined by imposing the condition $\Omega=\langle\omega\rangle_L$ in fully turbulent

regions.[15] It is observed that C_Ω varies around 0.9 with very small fluctuations. Therefore, we set $C_\Omega=0.9$. In Eq. (12d), $\hat{\omega}$ is the "local" frequency and is obtained as

$$\hat{\omega}=\hat{\epsilon}/k, \quad \hat{\epsilon}=C_f k^{3/2}/\Delta, \tag{15}$$

where k and $\hat{\omega}$ are evaluated on the finite-difference (FD) grid points [with $\tau(u_i,u_i)$ obtained from the Monte Carlo (MC) solver] and C_f is a model parameter. Considering the justifications and caveats[33,34] of using such a simple model for $\hat{\epsilon}$, it is adopted here because of its wide utilization in conventional LES.

The frequency model, Eq. (12d), is a relaxation equation that causes the stochastic frequency to relax to the local frequency $\hat{\omega}$. As C_ω increases, ω^+ converges faster to the local frequency $\hat{\omega}$. The sensitivity of the FVS-FMDF to model constants C_ω and C_f is discussed in Sec. V C.

The Fokker–Planck equation[35] which describes the transport of $F_L(\theta,\boldsymbol{v},\boldsymbol{\psi},\mathbf{x};t)$, the joint PDF of $\mathbf{X}^+$, $\boldsymbol{U}^+$, $\boldsymbol{\phi}^+$ and ω^+, is obtained from Eq. (12) as

$$\begin{aligned}\frac{\partial F_L}{\partial t}+\frac{\partial v_i F_L}{\partial x_i}&=\frac{\partial}{\partial x_j}\left[\mu\frac{\partial(F_L/\langle\rho\rangle_\ell)}{\partial x_j}\right]-\frac{\partial[S_\alpha(\boldsymbol{\psi})F_L]}{\partial\psi_\alpha}+\frac{1}{\langle\rho\rangle_\ell}\frac{\partial\langle p\rangle_\ell}{\partial x_i}\frac{\partial F_L}{\partial v_i}-\frac{2}{\langle\rho\rangle_\ell}\frac{\partial}{\partial x_j}\left(\mu\frac{\partial\langle u_i\rangle_L}{\partial x_j}\right)\frac{\partial F_L}{\partial v_i}-\frac{1}{\langle\rho\rangle_\ell}\frac{\partial}{\partial x_j}\left(\mu\frac{\partial\langle u_j\rangle_L}{\partial x_i}\right)\frac{\partial F_L}{\partial v_i}\\&+\frac{2}{3}\frac{1}{\langle\rho\rangle_\ell}\frac{\partial}{\partial x_i}\left(\mu\frac{\partial\langle u_j\rangle_L}{\partial x_j}\right)\frac{\partial F_L}{\partial v_i}-G_{ij}\frac{\partial[(v_j-\langle u_j\rangle_L)F_L]}{\partial v_i}+\frac{\partial}{\partial x_j}\left(\frac{2\mu}{\langle\rho\rangle_\ell}\frac{\partial\langle u_i\rangle_L}{\partial x_j}\frac{\partial F_L}{\partial v_i}\right)+\frac{\mu}{\langle\rho\rangle_\ell}\frac{\partial\langle u_i\rangle_L}{\partial x_k}\frac{\partial\langle u_j\rangle_L}{\partial x_k}\frac{\partial^2 F_L}{\partial v_i\,\partial v_j}\\&+\frac{1}{2}C_0 k\Omega\frac{\partial^2 F_L}{\partial v_i\,\partial v_i}+C_\phi\Omega\frac{\partial[(\psi_\alpha-\langle\phi_\alpha\rangle_L)F_L]}{\partial\psi_\alpha}+C_\omega\Omega\frac{\partial}{\partial\theta}[(\theta-\hat{\omega})F_L].\end{aligned} \tag{16}$$

The stochastic particle system, Eq. (12), aims to represent the fluid system, governed by Eqs. (1a)–(1c), at the level of one-point one-time statistics. Therefore, the PDF of the stochastic particle system is made to correspond with the PDF of SGS fields (the FVS-FMDF), i.e., $P_L(\theta,\boldsymbol{v},\boldsymbol{\psi},\mathbf{x};t)\equiv F_L(\theta,\boldsymbol{v},\boldsymbol{\psi},\mathbf{x};t)$. As a result, all the statistics obtained from the two systems are equivalent. This is shown in our previous works[12] and is not repeated here. The implied closure for the SDEs [Eq. (12)] is obtained by comparing the Fokker–Planck equation [Eq. (16)] to the FVS-FMDF exact transport equation [Eq. (11)]. The filtered frequency transport equation implied by the stochastic particle system, which is obtained from Eq. (16) by integration according to Eq. (9), is given by

$$\begin{aligned}\frac{\partial\langle\rho\rangle_\ell\langle\omega\rangle_L}{\partial t}+\frac{\partial\langle\rho\rangle_\ell\langle u_i\rangle_L\langle\omega\rangle_L}{\partial x_i}&=\frac{\partial}{\partial x_i}\left(\mu\frac{\partial\langle\omega\rangle_L}{\partial x_i}\right)\\&-\frac{\partial\langle\rho\rangle_\ell\tau(u_i,\omega)}{\partial x_i}\\&-C_\omega\Omega\langle\rho\rangle_\ell(\langle\omega\rangle_L-\hat{\omega}).\end{aligned} \tag{17}$$

IV. NUMERICAL SOLUTION PROCEDURE

A hybrid FD/MC scheme is employed to solve the coupled set of SDEs [Eq. (12)] and the filtered hydrodynamic equations. In this scheme, the domain is discretized by the FD grid points and the set of SDEs is solved by an ensemble of MC particles.[36] For simulations, the FDF is represented by an ensemble of N_p statistically identical MC particles. Each particle carries information pertaining to its position, $\mathbf{X}^{(n)}(t)$, frequency, $\omega^{(n)}(t)$, velocity, $\boldsymbol{U}^{(n)}(t)$, and scalar value, $\boldsymbol{\phi}^{(n)}(t)$, $n=1,\ldots,N_p$. This information is updated by integrating the corresponding SDEs, Eq. (12), over time via Euler–Maruyamma discretization.[37] For example, for Eq. (12a),

$$\begin{aligned}X_i^n(t_{k+1})=X_i^n(t_k)&+[D_i^X(t_k)]^n\Delta t+[B_{ij}^X(t_k)]^n(\Delta t)^{1/2}[\zeta_j^X(t_k)]^n\\&+[F_{ij}^{XU}(t_k)]^n(\Delta t)^{1/2}[\zeta_j^U(t_k)]^n\\&+[F_{ij}^{X\phi}(t_k)]^n(\Delta t)^{1/2}[\zeta_j^\phi(t_k)]^n,\end{aligned} \tag{18}$$

where $D_i(t_k)=D_i[\mathbf{X}^{(n)}(t_k),\boldsymbol{U}^{(n)}(t_k),\boldsymbol{\phi}^{(n)}(t_k);t_k],\ldots$ and $\zeta(t_k)$ are independent standardized Gaussian random variables. This scheme preserves the Itô character of the SDEs.[38] All of the hydrodynamic variables are determined on the FD grid points. A fourth order compact scheme is used for FD discretization of the flow equations, as described in Refs. 39 and 40. Transport of the MC particles and the change in their properties are described by the SDEs in Eq. (12). The MC particles are initially distributed randomly and are free to move within the domain. This transport is Lagrangian; thus the solution is free of the constraints associated with typical simulation of convection on fixed grid points. The filtered quantities are constructed on LES grid points by ensemble averaging over the particles in an ensemble domain as

$$\langle f\rangle_E\equiv\frac{1}{N_E}\sum_{n\in\Delta_E}f^{(n)}\underset{\substack{\Delta_E\to 0}}{\underset{N_E\to\infty}{\to}}\langle f\rangle_L, \tag{19}$$

where N_E denotes the number of MC particles residing within an ensemble domain of characteristic length Δ_E centered around each FD grid point. The particle variable $f^{(n)}$ denotes the information carried by nth MC particle pertaining to transport variable f. For reliable statistics with minimal numerical dispersion, it is desired to minimize the size of ensemble domain and maximize the number of the MC

particles.[26] In this way, the ensemble statistics would tend to the desired filtered values. Transfer of information from the grid points to the MC particles is accomplished by interpolation. The computational accuracy of the methodology is established by examining both the statistical and the dispersion errors.[41] In doing so, the correlation of the fluid density with MC particle distribution, the number of particles within the domain, and the global distribution of the particles are monitored in a manner similar to that reported in our previous works.[8–12] Reference 42 provides a detailed tutorial on the numerical simulation of the FDF.

The FD solver determines the pressure field which is further used in the MC solver. The filtered equations solved by the FD include unclosed moments which are obtained from the MC solver. The FD solver determines the filtered frequency, velocity, and scalar fields which are also obtained from the MC solver. That is, there is a "redundancy" in the determination of the first filtered moments as both the LES-FD and the MC procedures provide these fields. This redundancy is in fact very useful in monitoring the accuracy of the simulated results, as shown in our previous works.[9–12,43,44]

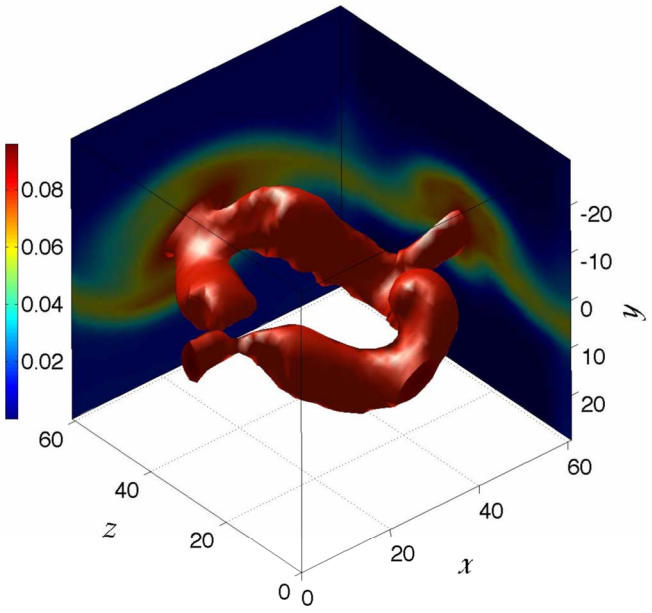

FIG. 1. (Color online) The instantaneous isosurface of the filtered frequency ($\langle\omega\rangle_L$=0.083) at time t=80.

V. RESULTS

A. Flow simulated and numerical specifications

The flow configuration considered is a 3D temporally developing mixing layer. This flow consists of two parallel streams traveling in opposite directions with the same speed.[45–47] In the representation below, u, v, and w are the velocity components in the x (streamwise), y (cross-stream), and z (spanwise) directions, respectively. The filtered streamwise velocity, density, and passive scalar fields are initialized using hyperbolic tangent profiles with free-stream conditions as $\langle u\rangle_L=1$, $\langle\rho\rangle_\ell=0.5$, and $\langle\phi\rangle_L=1$ on the top and $\langle u\rangle_L=-1$, $\langle\rho\rangle_\ell=1$, and $\langle\phi\rangle_L=0$ on the bottom. Simulations are conducted on a cubic box, $0\le x\le L$, $-L/2\le y\le L/2$, $0\le z\le L$ where L is the normalized length specified as $L=2^{N_v}\lambda_u/L_r$, where N_v is the desired number of successive vortex pairings and λ_u is the wavelength of the most unstable mode corresponding to the mean streamwise velocity profile imposed at the initial time. The flow variables are normalized with respect to the reference length L_r defined as one-half the initial vorticity thickness, and the reference velocity, defined as one-half the velocity difference across the layer. The Reynolds number based on these reference values is $\mathrm{Re}=U_rL_r/\nu=50$. The flow is initialized similar to that in Ref. 48 and is assessed by comparing with the data obtained by DNS of the same flow. Simulations are performed on 33^3 and 193^3 equally spaced grid points for LES and DNS, respectively. The grid spacing is the same in all directions and the LES filter size is twice as large as the grid spacing in each direction. To filter the DNS data, a top-hat function with the width equal to the LES filter size is used. The periodic boundary condition is used in the streamwise and spanwise directions and zero-derivative boundary condition is used at cross-stream boundaries. The MC particles have variable weights, as described in our previous works,[9,12] and are distributed uniformly throughout the computational domain in a random fashion. The initial number of particles per grid point is 320 and the ensemble domain size is set equal to one-half the grid spacing in each direction. The initialization of the particles and their treatment at the boundaries are consistent with the FD initial and boundary conditions. A spatial perturbation is used at the initial time which causes the formation of 3D large scale structures. This is demonstrated in Fig. 1 which shows the turbulent regions of the layer at time t=80. In regions where frequency has lower values, the flow is laminar, whereas high values denote turbulent regions of the layer. In this figure, the formation of large scale structures in the spanwise and the streamwise directions is clearly evident.

B. Model assessment

Since the accuracy of the FD results is well established, the consistency check gives a useful assessment of the accuracy of the MC solver. The consistency of the velocity and the scalar statistics is established in our previous works.[8–12] Here, the consistency of the frequency statistics is demonstrated. The filtered frequency obtained from the MC solver by ensemble averaging [Eq. (19)] is compared with that obtained by solving Eq. (17) directly using FD. Figure 2 shows the scatter plot of filtered frequency obtained from both solvers. The consistency is demonstrated by the high value of the correlation coefficient.

One of the advantages of the FVS-FMDF is its capability to take the history of particles into account. To demonstrate this, the MC particles are tagged in the simulations based on their original locations. Figure 3 shows the frequency of MC particles near the center plane. The fully turbulent region is located near the center (y=0) where the value of frequency is the highest. Away from the center, the intermittent flow regions are evident as the turbulent (high frequency) and nonturbulent (low frequency) particles coex-

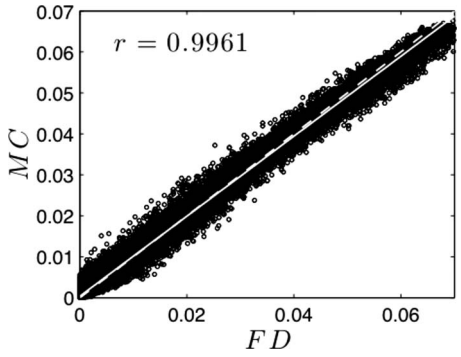

FIG. 2. Consistency of instantaneous filtered frequency obtained from FD and MC at time $t=80$. The solid and dashed lines denote the linear regression and the 45° lines, respectively. r denotes the correlation coefficient. The circles denote the filtered frequency values on the FD grid points.

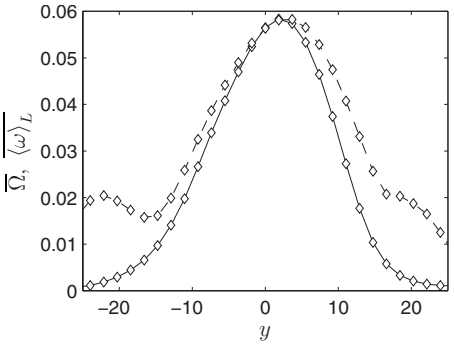

FIG. 4. Reynolds-averaged filtered (solid line) and SGS mixing (dashed line) frequency values obtained from FVS-FMDF ($C_f=1$, $C_\omega=1$) simulations at time $t=80$.

ist. The PDF of particle frequency in these regions is bimodal.[1,15] As this figure demonstrates, the particles originating from high-speed stream penetrate deep into the low-speed stream and vice versa. In this figure, the frequency $\hat{\omega}$ [obtained from Eq. (15) on the FD grid points] is superimposed on particles. It is clear that the particles do not immediately take the local frequency values. Instead, they retain their original information as they move throughout the domain. The FVS-FMDF accounts for the origin of MC particles; thus it provides a more realistic representation of the fluid particles.

Figure 4 shows the SGS mixing frequency, defined as the conditional filtered frequency [Eq. (14)], and the filtered frequency. As shown, the two quantities are equal near the center of the layer where the frequency is the highest (fully turbulent region). This is due to the specification of C_Ω, as discussed in Sec. III C. Near the edges where the filtered frequency is almost zero, the conditional filtered frequency has finite values. Due to the intermittent nature of the flow in these regions, as shown in Fig. 3, both turbulent and nonturbulent particles are present. The conditional filtered frequency only takes the turbulent particles into account when ensemble averaging in these regions.[15] This quantity is shown to be a more proper representative of the SGS mixing frequency. Employment of conditional filtered frequency causes the relative magnitude of dissipation to increase in the edges of the layer.[15] This is advantageous as it reduces the level of numerical fluctuations in particle quantities. As an example, in Fig. 5, a comparison of scatter plots is made from three different simulations. Figure 5(a) corresponds to the FVS-FMDF simulations in which the conditional filtered frequency is used. Figures 5(b) and 5(c) are obtained from the FVS-FMDF simulations in which the SGS mixing frequency is substituted by the filtered frequency and the local frequency, respectively. As demonstrated, the particles in simulations with the conditional filtered frequency show the smallest level of fluctuations near the edges. Although this has little effect on the low order moments, it improves the higher order moments significantly as shown in Fig. 6. In this figure, in spite of close agreements between the filtered velocity fields, the SGS kinetic energy predicted via $\langle\omega\rangle_L$ shows unrealistic increase near the edges where the flow is nearly laminar. The other two simulations provide more accurate predictions of the SGS kinetic energy in these regions.

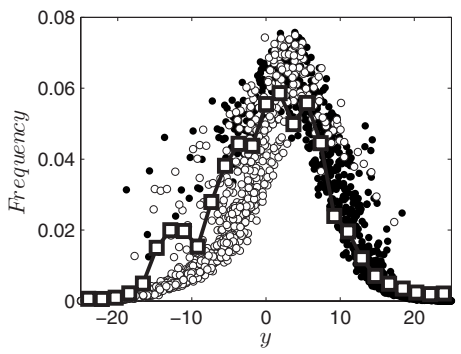

FIG. 3. Cross-stream variation of particle frequency values near the $x=z=30$ plane at time $t=80$. The white and black circles denote particles originated in low-speed and high-speed streams, respectively. The squares denote the frequency $\hat{\omega}$ [Eq. (15)] values on the FD grid points.

C. Comparative assessments of the FVS-FMDF

In this section we make *a posteriori* analysis of some of the characteristics of the FVS-FMDF by comparing the results against DNS data. This assessment is to evaluate the final results predicted by the FVS-FMDF and to determine the range of frequency model parameters. In addition to FVS-FMDF, LES is also conducted using the Smagorinsky[19] SGS closure as employed by Moin *et al.*[49]

In the following presentation, the "Reynolds-averaged" statistics, shown by an overbar, are obtained by averaging the instantaneous results over the homogeneous (x,z) directions. Figures 7(a) and 7(b) show the Reynolds-averaged values of the streamwise velocity and the passive scalar. Several values of the model parameters C_f and C_ω are considered. The influence of other model parameters are assessed in our previous studies.[8–11] It is observed that the first moments are almost insensitive to these parameters. All the FVS-FMDF results show good agreements with the DNS data. However, with the Smagorinsky model, the thickness of the layer is underpredicted. This is also evident in Figs. 7(c) and 7(d) which show the time variation of momentum thickness,[50]

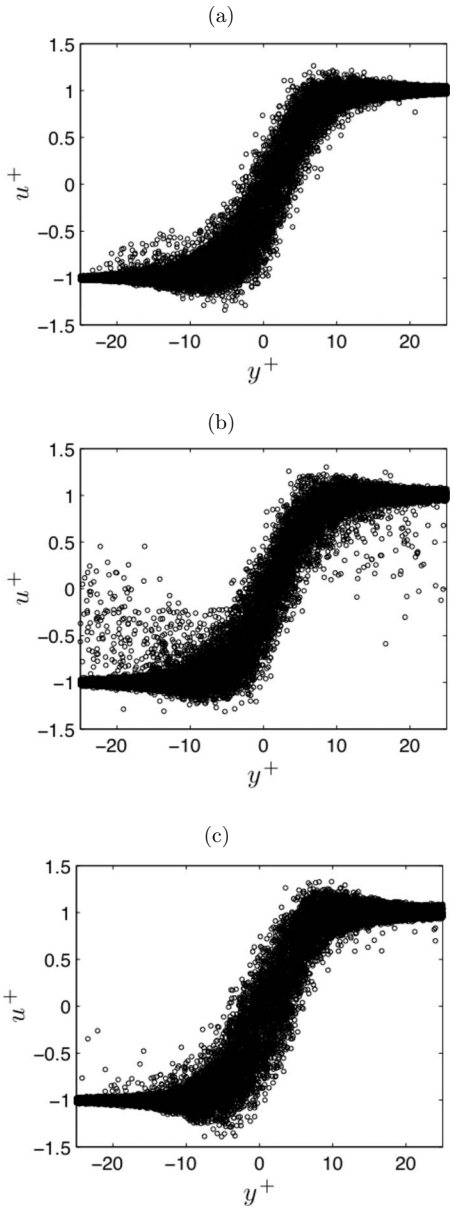

FIG. 5. Particle streamwise velocity values obtained from simulations with the SGS mixing frequency defined as (a) conditional filtered frequency Ω, (b) $\langle\omega\rangle_L$, and (c) $\hat{\omega}$ [Eq. (15)]. These particles are collected near the $z=20$ plane at time $t=80$.

$$\delta(t) = \frac{1}{\rho_1(\Delta u)^2}\int_{-\infty}^{+\infty} \overline{\langle\rho\rangle_\ell}(u_1 - \overline{\langle u\rangle_L})(\overline{\langle u\rangle_L} - u_2)dy \tag{20}$$

(where $\Delta u = u_1 - u_2$, u_1 and u_2 are the top and bottom free-stream streamwise velocity components, respectively, and ρ_1 is the top free-stream density) and the scalar thickness,

$$\delta_s(t) = y(\overline{\langle\phi\rangle_L} = 0.9) - y(\overline{\langle\phi\rangle_L} = 0.1). \tag{21}$$

With the Smagorinsky model, these thicknesses are slightly overpredicted initially and underpredicted significantly later on. All the FVS-FMDF cases yield almost similar prediction of the layer's growth rate. The frequency model plays a crucial role in the evolution of the layer through its description of turbulent dissipation and SGS mixing frequency. To further analyze the behavior of the SGS models, the following integral quantities are considered:

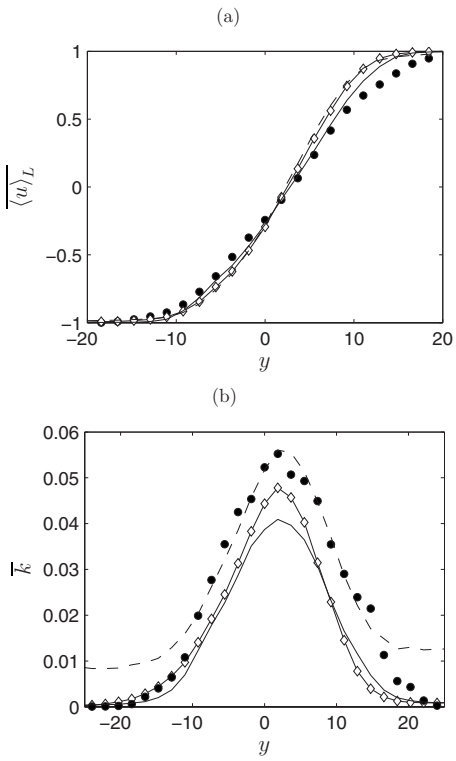

FIG. 6. Reynolds-averaged (a) filtered streamwise velocity and (b) SGS kinetic energy at time $t=80$. The results obtained from simulations with the SGS mixing frequency defined as $\hat{\omega}$ (solid line), $\langle\omega\rangle_L$ (dashed line), and Ω (symbol $\diamond$). The black circles denote filtered DNS data.

$$\begin{aligned}
E_k(t) &= \int \frac{1}{2}\langle u_i\rangle_L\langle u_i\rangle_L d\mathbf{x},\\
P_k(t) &= \int p_k d\mathbf{x}, \quad p_k = -\langle\rho\rangle_\ell \tau(u_i,u_j)\frac{\partial\langle u_i\rangle_L}{\partial x_j},\\
D_k(t) &= \int \epsilon_v d\mathbf{x}, \quad \epsilon_v = S_{ij}\langle\tau_{ij}\rangle_L,\\
B_k(t) &= \int \min(0,p_k)d\mathbf{x},
\end{aligned} \tag{22}$$

where E_k is the resolved kinetic energy, P_k is the SGS dissipation (or the production rate of SGS kinetic energy which is the rate of energy transfer from resolved to SGS scales), D_k denotes the resolved dissipation rate (which is the rate of energy dissipation from the resolved field by molecular viscosity), and B_k is the total backscatter (defined as the rate of energy transfer from the SGS back to the resolved scales[51]). These integral quantities are shown in Fig. 8. Consistent with Fig. 7, the resolved kinetic energy is underpredicted by the Smagorinsky model initially and overpredicted at later times. As Fig. 8(b) shows, the high SGS dissipation associated with this model in the transitional stages hinders the development of small scale vortical structures, which consequently causes the underprediction of the SGS dissipation. The resolved dis-

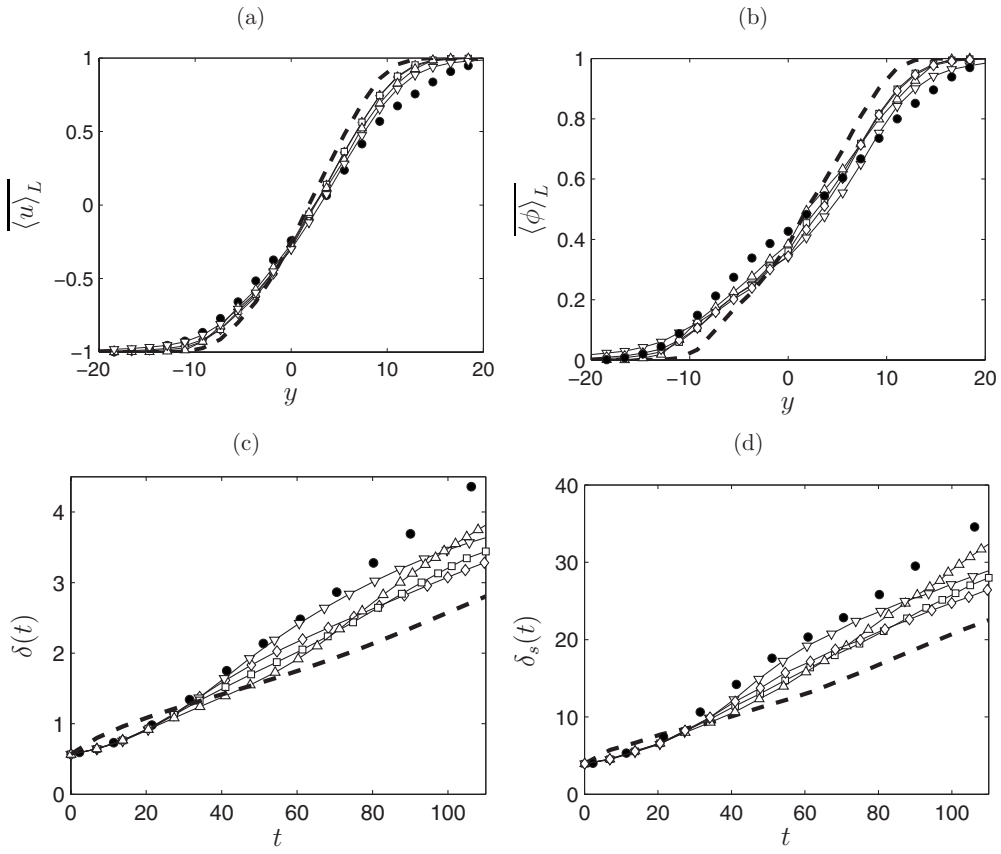

FIG. 7. Cross-stream variation of Reynolds-averaged filtered (a) streamwise velocity and (b) passive scalar; temporal variation of (c) momentum thickness and (d) scalar thickness of the shear layer. The predictions are obtained from DNS, the FVS-FMDF, and the Smagorinsky model. The dashed lines denote the Smagorinsky predictions. The symbols denote (▽) FVS-FMDF (C_f=0.5, C_ω=2), (◇) FVS-FMDF (C_f=1, C_ω=1), (□) FVS-FMDF (C_f=1, C_ω=2), (△) FVS-FMDF (C_f=2, C_ω=1), and (●) filtered DNS data.

sipation values are, in general, lower than those of the SGS dissipation. As Fig. 8 demonstrates, the initial development of the layer is more accurately predicted by the FVS-FMDF. The SGS dissipation depends more strongly on the frequency model parameters: as C_f decreases, the peak magnitude increases which causes increased decay rate of resolved kinetic energy. The resolved dissipation is predicted similarly by the FVS-FMDF regardless of the model parameter values. The exception is C_f=2 which causes an increase in this quantity at late times. By definition, the Smagorinsky model does not represent the backscatter. The FVS-FMDF is capable of predicting the backscatter, as shown in Fig. 8(d), without any numerical instability problems.[52,53] With the model parameters chosen, the backscatter values are generally much smaller than those predicted by DNS. As Figs. 8(b) and 8(d) suggest, as C_f decreases peak magnitudes of both SGS dissipation and backscatter increase.

The SGS kinetic energy and several components of SGS stress and SGS scalar flux tensors are shown in Figs. 9 and 10. The FVS-FMDF provides satisfactory predictions of SGS fields. The Smagorinsky model underpredicts these stresses. An exception is the scalar flux $\tau(v,\phi)$, which is predicted well by the Smagorinsky model and the FVS-FMDF (with C_f=2 and C_ω=1). While the SGS fields are less sensitive to the C_ω value, lowering C_f results in significant overprediction of SGS fields. With C_f=0.5 and C_ω=2 the SGS contribution is a large fraction of the total stresses which is unsuitable for LES. Figures 11–14 show several components of Reynolds-averaged "resolved" and "total" stress and scalar flux tensors. The former is $\overline{R(a,b)}$ with $R(a,b)=(\langle a\rangle_L - \overline{\langle a\rangle_L})(\langle b\rangle_L - \overline{\langle b\rangle_L})$ and the latter is $\overline{r(a,b)}$ with $r(a,b)=(a-\bar{a})(b-\bar{b})$. In DNS, the total components are directly available, while in LES they are approximated by $\overline{r(a,b)} \approx \overline{R(a,b)} + \overline{\tau(a,b)}$.[48] The Smagorinsky model underpredicts both spread and peak values of the resolved and the total fields. The FVS-FMDF (with C_f=2 and C_ω=1) provides close agreements with DNS data. Small C_f values result in decreased resolved fields. However, large C_ω values cause the resolved fields to increase. The most accurate overall FVS-FMDF predictions are obtained with C_f=2 and C_ω=1. The model parameters C_f and C_ω have insignificant influence on the first order moments. However, although the SGS and resolved contributions are quite sensitive to these parameters, the total fields show relatively less variations. This is consistent with our previous works.[10–12]

VI. SUMMARY AND CONCLUDING REMARKS

The FDF methodology has proven very effective for the simulation of turbulent reacting flows. In previous investigations, the marginal FDF of the scalar, that of the velocity, and the joint VSFDF were considered. All these methodologies are somewhat deficient in providing accurate information on the SGS time or length scales. The objective of the present

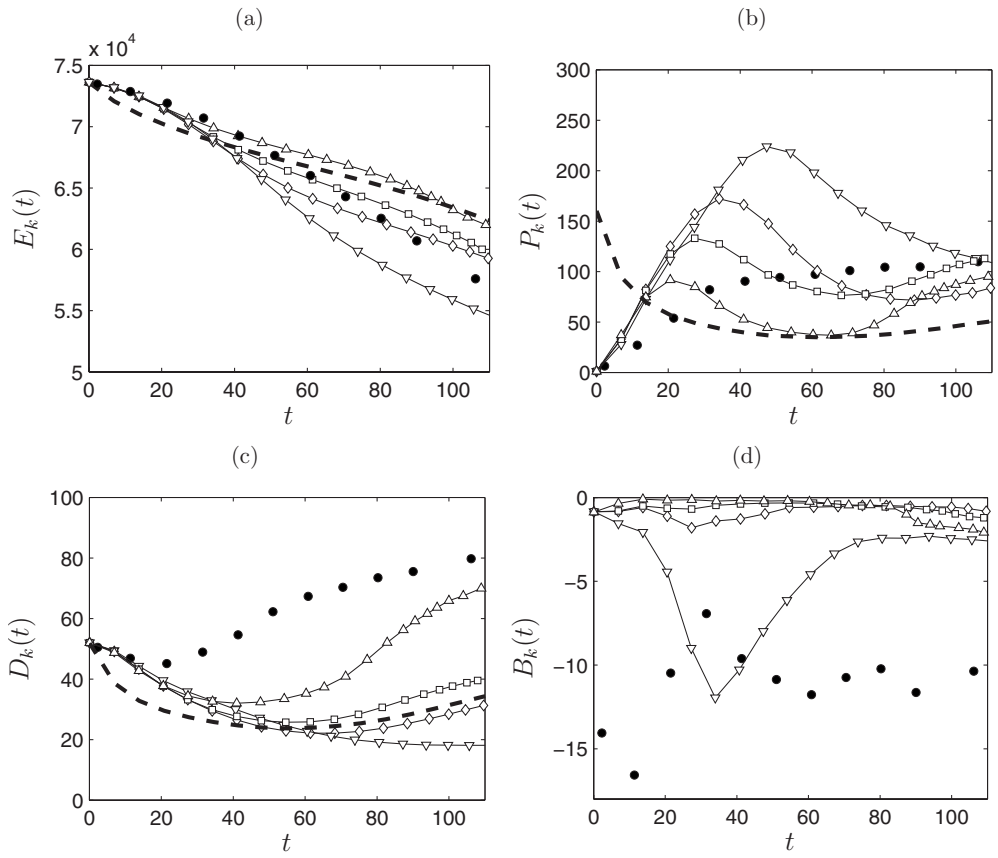

FIG. 8. Temporal variation of (a) resolved kinetic energy, (b) SGS dissipation, (c) resolved dissipation, and (d) backscatter predicted by DNS and LES using the FVS-FMDF and the Smagorinsky model. The dashed lines denote the Smagorinsky model predictions. The symbols denote (▽) FVS-FMDF (C_f=0.5, C_ω=2), (◇) FVS-FMDF (C_f=1, C_ω=1), (□) FVS-FMDF (C_f=1, C_ω=2), (△) FVS-FMDF (C_f=2, C_ω=1), and (●) filtered DNS data.

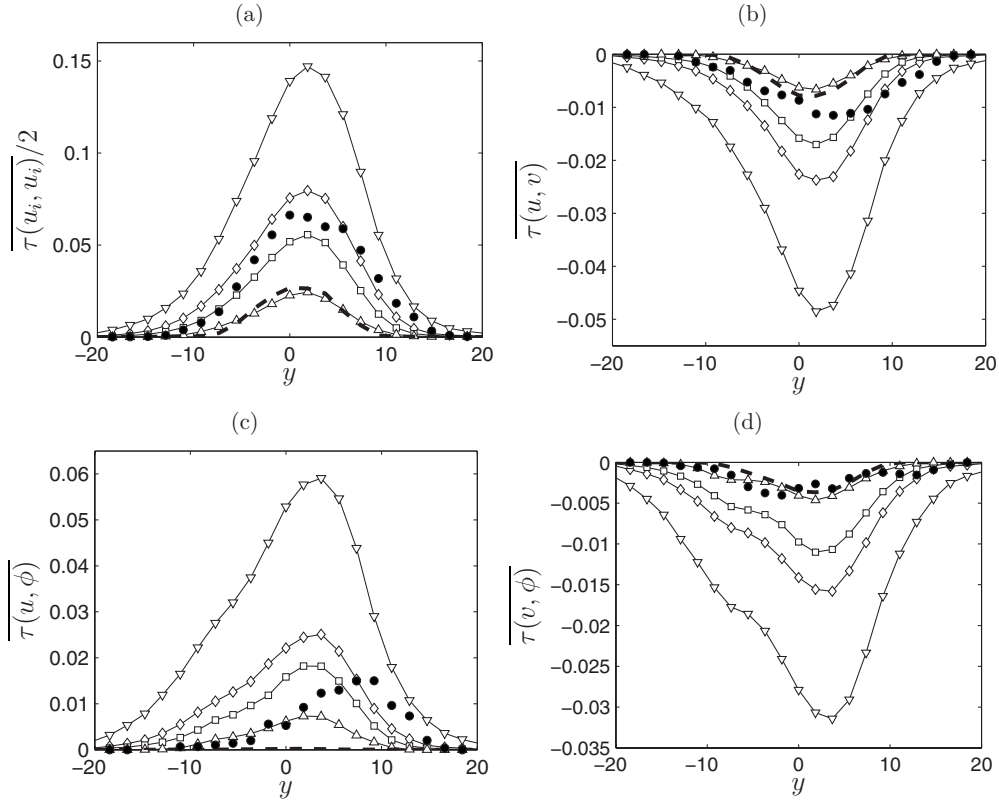

FIG. 9. Reynolds-averaged SGS kinetic energy and components of SGS stress and SGS scalar flux tensors obtained at time t=60. The dashed lines denote the Smagorinsky model predictions. The symbols denote (▽) FVS-FMDF (C_f=0.5, C_ω=2), (◇) FVS-FMDF (C_f=1, C_ω=1), (□) FVS-FMDF (C_f=1, C_ω=2), (△) FVS-FMDF (C_f=2, C_ω=1), and (●) filtered DNS data.

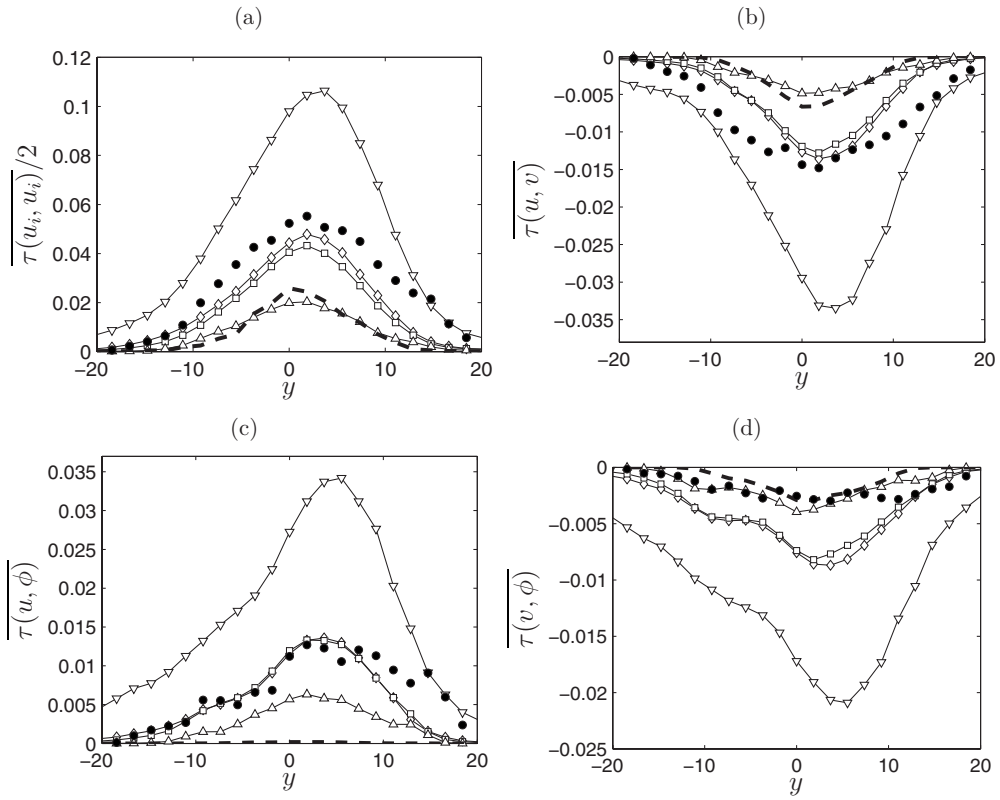

FIG. 10. Reynolds-averaged SGS kinetic energy and components of SGS stress and SGS scalar flux tensors obtained at time $t=80$. The dashed lines denote the Smagorinsky model predictions. The symbols denote (▽) FVS-FMDF ($C_f=0.5, C_\omega=2$), (◇) FVS-FMDF ($C_f=1$, $C_\omega=1$), (□) FVS-FMDF ($C_f=1$, $C_\omega=2$), (△) FVS-FMDF ($C_f=2$, $C_\omega=1$), and (●) filtered DNS data.

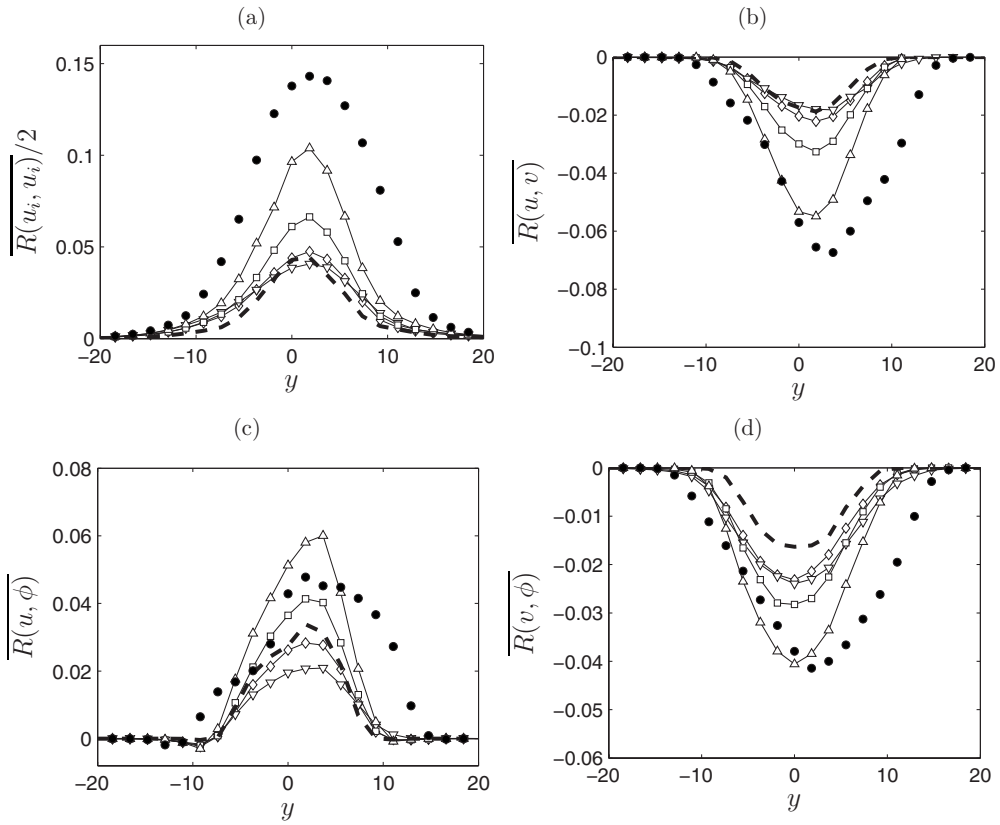

FIG. 11. Reynolds-averaged resolved kinetic energy and components of resolved stress and resolved scalar flux tensors obtained at time $t=60$. The dashed lines denote the Smagorinsky model predictions. The symbols denote (▽) FVS-FMDF ($C_f=0.5, C_\omega=2$), (◇) FVS-FMDF ($C_f=1$, $C_\omega=1$), (□) FVS-FMDF ($C_f=1$, $C_\omega=2$), (△) FVS-FMDF ($C_f=2$, $C_\omega=1$), and (●) filtered DNS data.

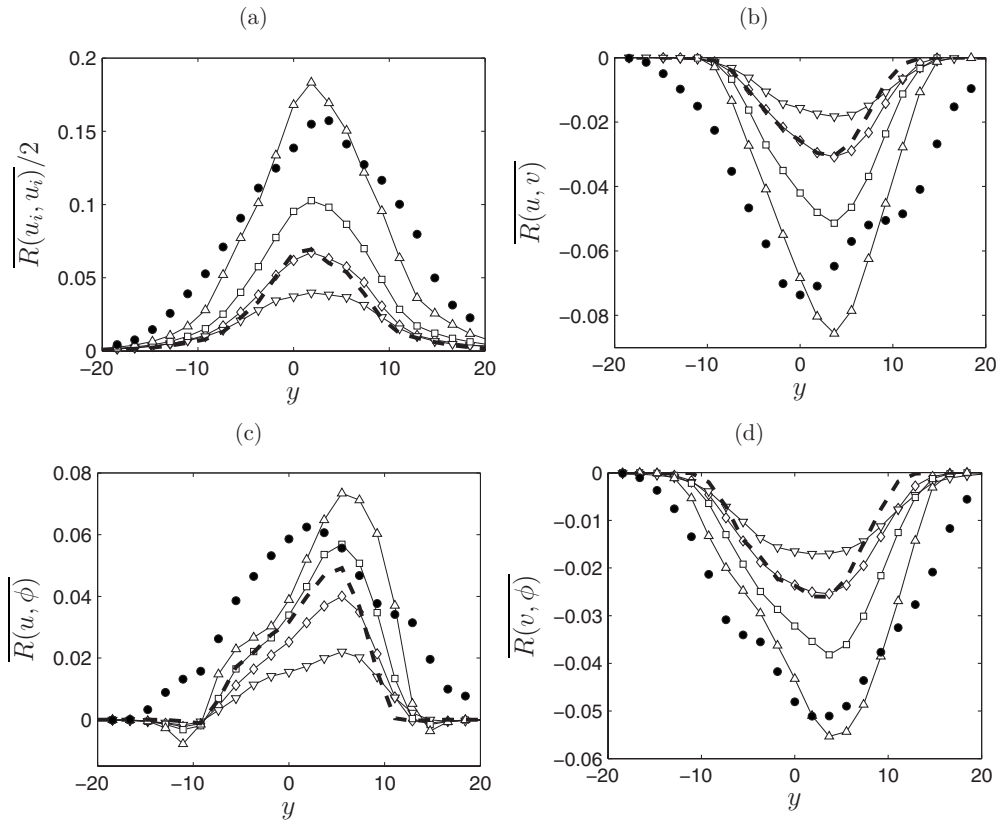

FIG. 12. Reynolds-averaged resolved kinetic energy and components of resolved stress and resolved scalar flux tensors obtained at time $t=80$. The dashed lines denote the Smagorinsky model predictions. The symbols denote (▽) FVS-FMDF ($C_f=0.5, C_\omega=2$), (◇) FVS-FMDF ($C_f=1,\ C_\omega=1$), (□) FVS-FMDF ($C_f=1,\ C_\omega=2$), (△) FVS-FMDF ($C_f=2,\ C_\omega=1$), and (●) filtered DNS data.

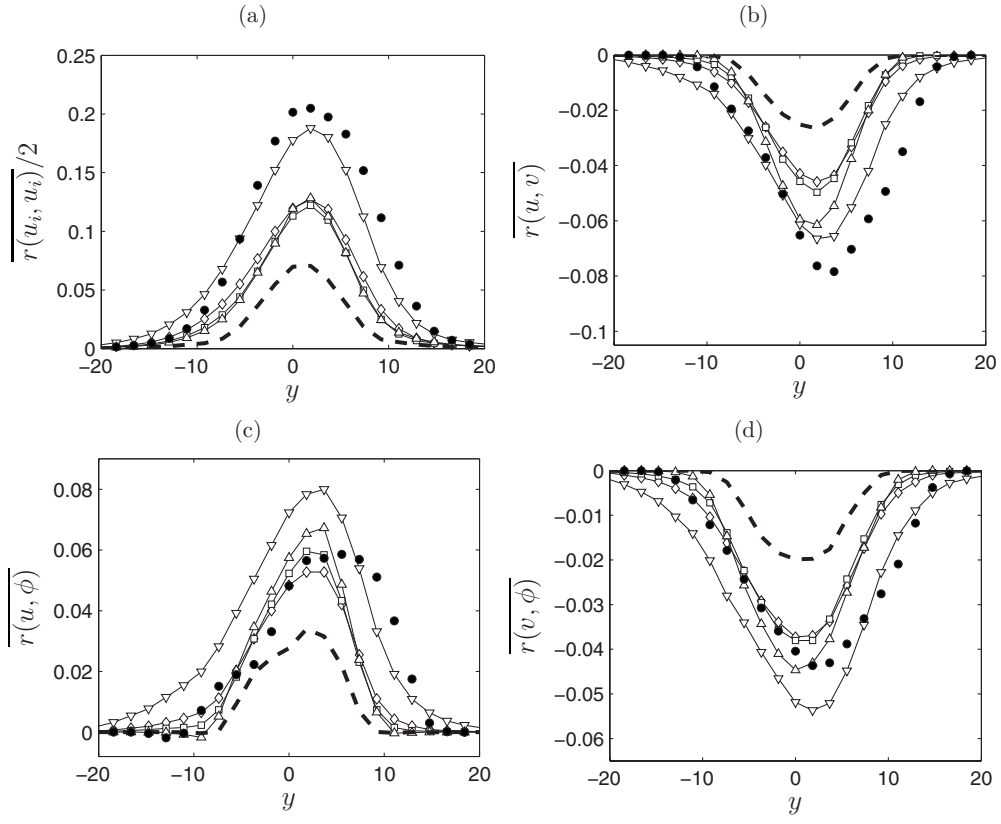

FIG. 13. Reynolds-averaged total kinetic energy and components of total stress and total scalar flux tensors obtained at time $t=60$. The dashed lines denote the Smagorinsky model predictions. The symbols denote (▽) FVS-FMDF ($C_f=0.5, C_\omega=2$), (◇) FVS-FMDF ($C_f=1,\ C_\omega=1$), (□) FVS-FMDF ($C_f=1,\ C_\omega=2$), (△) FVS-FMDF ($C_f=2,\ C_\omega=1$), and (●) filtered DNS data.

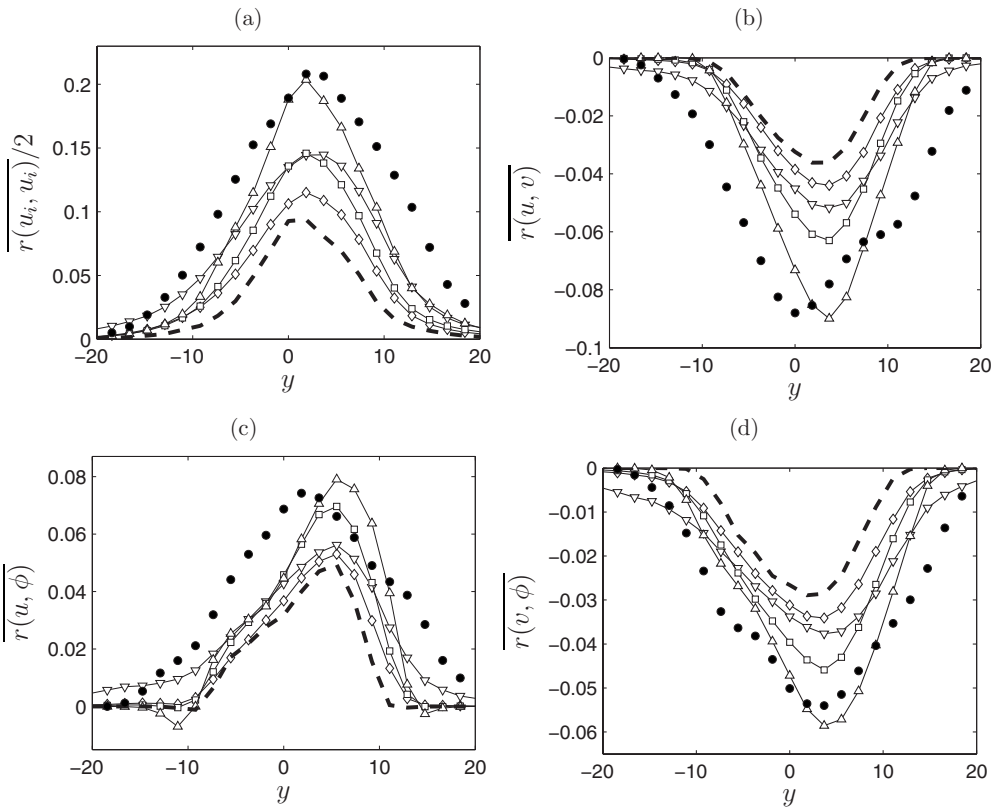

FIG. 14. Reynolds-averaged total kinetic energy and components of total stress and total scalar flux tensors obtained at time $t=80$. The dashed lines denote the Smagorinsky model predictions. The symbols denote (▽) FVS-FMDF ($C_f=0.5, C_\omega=2$), (◇) FVS-FMDF ($C_f=1,\ C_\omega=1$), (□) FVS-FMDF ($C_f=1,\ C_\omega=2$), (△) FVS-FMDF ($C_f=2,\ C_\omega=1$), and (●) filtered DNS data.

work is to address this deficiency by including the transport of the frequency within the FDF framework. The resulting formulation contains the complete statistical information on joint frequency, velocity, and scalar fields and is entitled "frequency-velocity-scalar filtered mass density function" (FVS-FMDF). The FVS-FMDF is governed by an exact transport equation which is derived from the Navier–Stokes and the scalars' transport equations. In FVS-FMDF transport equation, the effects of convection and chemical reactions are in closed forms. The unclosed terms are modeled in a fashion similar to those typically followed in PDF methods in RANS simulations. The modeled FVS-FMDF transport equation, which is based on a set of SDEs, is solved numerically by a Lagrangian MC solution procedure.

The FVS-FMDF is applied to a 3D temporally developing mixing layer involving the transport of a passive scalar. To assess the performance of the FVS-FMDF, DNS is also conducted of the same flow. The FVS-FMDF results are also compared with those obtained from LES via the Smagorinsky[19] SGS closure. The FVS-FMDF prediction of the first two SGS moments is shown to be in reasonable agreements with the DNS data. The sensitivity of the FVS-FMDF results with respect to frequency model parameters ($C_f,\ C_\omega$) is studied. Consistent with our previous works,[8–12] it is shown that the variation of filtered quantities (the first order moments) with model parameters is small. The SGS and resolved contribution of second order moments show more sensitivity. However, the total second order moments vary relatively less with the model parameters. Obviously, the values cannot be set in such a way that the contribution of the SGS components to the total components becomes too large.

Some suggestions for possible future work are as follows:

- Implementation of higher order closures for the generalized Langevin model parameter G_{ij}.[30] The model parameter considered here correspond to Rotta's closure in RANS.[1,54] Higher order closure similar to those considered in RANS[28,30] may be implemented.
- Extension of the FDF methodology to account for differential diffusion effects.[55–61] The FVS-FMDF may be extended to flows with nonunity Prandtl and/or Schmidt numbers. It may also be extended to include temperature dependent viscosity and diffusion coefficients.
- Extension of the FVS-FMDF for simulation of complex flows. The SFDF has proven very effective in LES of turbulent flames.[3–7] It is recommended to implement the FVS-FMDF for prediction of these flames.

ACKNOWLEDGMENTS

This work is sponsored by NASA under Grant No. NNX08AB36A and the U.S. Air Force Office of Scientific Research with Dr. Julian M. Tishkoff as the Program Manager under Grant No. FA9550-06-1-0015 to University of

Pittsburgh and Grant No. FA9550-09-1-0047 to Cornell University. The computational support is provided by the National Science Foundation through TeraGrid resources at Pittsburgh Supercomputing Center.

[1]S. B. Pope, *Turbulent Flows* (Cambridge University Press, Cambridge, 2000).
[2]P. Givi, "Filtered density function for subgrid scale modeling of turbulent combustion," AIAA J. **44**, 16 (2006).
[3]M. R. H. Sheikhi, T. G. Drozda, P. Givi, F. A. Jaberi, and S. B. Pope, "Large eddy simulation of a turbulent nonpremixed piloted methane jet flame (Sandia flame D)," Proc. Combust. Inst. **30**, 549 (2005).
[4]T. G. Drozda, M. R. H. Sheikhi, C. K. Madnia, and P. Givi, "Developments in formulation and application of the filtered density function," Flow, Turbul. Combust. **78**, 35 (2007).
[5]S. James, J. Zhu, and M. S. Anand, "Large eddy simulations of turbulent flames using the filtered density function model," Proc. Combust. Inst. **31**, 1737 (2007).
[6]V. Raman, H. Pitsch, and R. O. Fox, "Hybrid large-eddy simulation/Lagrangian filtered density function approach for simulating turbulent combustion," Combust. Flame **143**, 56 (2005).
[7]V. Raman, H. Pitsch, and A. Consistent, "LES/filtered-density function formulation for the simulation of turbulent flames with detailed chemistry," Proc. Combust. Inst. **31**, 1711 (2007).
[8]P. J. Colucci, F. A. Jaberi, P. Givi, and S. B. Pope, "Filtered density function for large eddy simulation of turbulent reacting flows," Phys. Fluids **10**, 499 (1998).
[9]F. A. Jaberi, P. J. Colucci, S. James, P. Givi, and S. B. Pope, "Filtered mass density function for large eddy simulation of turbulent reacting flows," J. Fluid Mech. **401**, 85 (1999).
[10]L. Y. M. Gicquel, P. Givi, F. A. Jaberi, and S. B. Pope, "Velocity filtered density function for large eddy simulation of turbulent flows," Phys. Fluids **14**, 1196 (2002).
[11]M. R. H. Sheikhi, T. G. Drozda, P. Givi, and S. B. Pope, "Velocity-scalar filtered density function for large eddy simulation of turbulent flows," Phys. Fluids **15**, 2321 (2003).
[12]M. R. H. Sheikhi, P. Givi, and S. B. Pope, "Velocity-scalar filtered mass density function for large eddy simulation of turbulent reacting flows," Phys. Fluids **19**, 095106 (2007).
[13]S. B. Pope, "Application of the velocity-dissipation probability density function model in inhomogeneous turbulent flows," Phys. Fluids A **3**, 1947 (1991).
[14]P. R. Van Slooten and S. B. Pope, "Application of PDF modeling to swirling and nonswirling turbulent jets," Flow, Turbul. Combust. **62**, 295 (1999).
[15]P. R. Van Slooten, Jayesh, and S. B. Pope, "Advances in PDF modeling for inhomogeneous turbulent flows," Phys. Fluids **10**, 246 (1998).
[16]S. B. Pope and Y. L. Chen, "The velocity-dissipation probability density function model for turbulent flows," Phys. Fluids A **2**, 1437 (1990).
[17]S. B. Pope and D. C. Haworth, in *Turbulent Shear Flows 5*, edited by F. Durst, B. E. Launder, F. W. Schmidt, and J. H. Whitelaw (Springer-Verlag, Berlin, 1987), pp. 44–53.
[18]S. B. Pope, "Lagrangian PDF methods for turbulent flows," Annu. Rev. Fluid Mech. **26**, 23 (1994).
[19]J. Smagorinsky, "General circulation experiments with the primitive equations. I. The basic experiment," Mon. Weather Rev. **91**, 99 (1963).
[20]F. A. Williams, *Combustion Theory*, 2nd ed. (Benjamin Cummings, Menlo Park, 1985).
[21]U. Piomelli, "Large-eddy simulation: Achievements and challenges," Prog. Aerosp. Sci. **35**, 335 (1999).
[22]C. Meneveau and J. Katz, "Scale-invariance and turbulence models for large-eddy simulations," Annu. Rev. Fluid Mech. **32**, 1 (2000).
[23]*Modern Simulation Strategies for Turbulent Flow*, edited by B. J. Geurts (Edwards, Philadelphia, 2001).
[24]P. Sagaut, *Large Eddy Simulation for Incompressible Flows*, 2nd ed. (Springer-Verlag, New York, 2002).
[25]E. E. O'Brien, in *Turbulent Reacting Flows*, edited by P. A. Libby and F. A. Williams (Springer-Verlag, Heidelberg, 1980), Chap. 5, pp. 185–218.
[26]S. B. Pope, "PDF methods for turbulent reactive flows," Prog. Energy Combust. Sci. **11**, 119 (1985).
[27]C. W. Gardiner, *Handbook of Stochastic Methods* (Springer-Verlag, New York, 1990).
[28]D. C. Haworth and S. B. Pope, "A generalized Langevin model for turbulent flows," Phys. Fluids **29**, 387 (1986).
[29]T. D. Dreeben and S. B. Pope, "Probability density function and Reynolds-stress modeling of near-wall turbulent flows," Phys. Fluids **9**, 154 (1997).
[30]S. B. Pope, "On the relation between stochastic Lagrangian models of turbulence and second-moment closures," Phys. Fluids **6**, 973 (1994).
[31]C. Dopazo, in *Turbulent Reacting Flows*, edited by P. A. Libby and F. A. Williams (Academic, London, 1994), Chap. 7, pp. 375–474.
[32]R. Borghi, "Turbulent combustion modeling," Prog. Energy Combust. Sci. **14**, 245 (1988).
[33]S. G. Chumakov, "Scaling properties of subgrid-scale energy dissipation," Phys. Fluids **19**, 058104 (2007).
[34]C. Meneveau and J. O'Neil, "Scaling laws of the dissipation rate of turbulent subgrid-scale kinetic energy," Phys. Rev. E **49**, 2866 (1994).
[35]H. Risken, *The Fokker–Planck Equation, Methods of Solution and Applications* (Springer-Verlag, New York, 1989).
[36]S. B. Pope, "Particle method for turbulent flows: Integration of stochastic model equations," J. Comput. Phys. **117**, 332 (1995).
[37]P. E. Kloeden, E. Platen, and H. Schurz, *Numerical Solution of Stochastic Differential Equations Through Computer Experiments*, corrected 2nd printing ed. (Springer-Verlag, New York, 1997).
[38]I. I. Gikhman and A. V. Skorokhod, *Stochastic Differential Equations* (Springer-Verlag, New York, 1972).
[39]J. P. Drummond, M. H. Carpenter, and D. W. Riggins, in *High Speed Propulsion Systems*, AIAA Progress Series, edited by S. N. B. Murthy and E. T. Curran (American Institute of Aeronautics and Astronautics, Reston, VA, 1991), Vol. 137, Chap. 7, pp. 383–455.
[40]C. A. Kennedy and M. H. Carpenter, "Several new numerical methods for compressible shear-layer simulations," Appl. Numer. Math. **14**, 397 (1994).
[41]J. Xu and S. B. Pope, "Assessment of numerical accuracy of PDF/Monte Carlo methods for turbulent reacting flows," J. Comput. Phys. **152**, 192 (1999).
[42]C. K. Madnia, F. A. Jaberi, and P. Givi, in *Handbook of Numerical Heat Transfer*, 2nd ed., edited by W. J. Minkowycz, E. M. Sparrow, and J. Y. Murthy (Wiley, New York, 2006), Chap. 5, pp. 167–189.
[43]M. Muradoglu, P. Jenny, S. B. Pope, and D. A. Caughey, "A consistent hybrid-volume/particle method for the PDF equations of turbulent reactive flows," J. Comput. Phys. **154**, 342 (1999).
[44]M. Muradoglu, S. B. Pope, and D. A. Caughey, "The hybrid method for the PDF equations of turbulent reactive flows: Consistency conditions and correction algorithms," J. Comput. Phys. **172**, 841 (2001).
[45]J. J. Riley and R. W. Metcalfe, "Direct numerical simulations of a perturbed, turbulent mixing layer," AIAA Paper No. 80-0274, 1980.
[46]N. D. Sandham and W. C. Reynolds, "Three-dimensional simulations of large eddies in the compressible mixing layer," J. Fluid Mech. **224**, 133 (1991).
[47]R. D. Moser and M. M. Rogers, "The three-dimensional evolution of a plane mixing layer: Pairing and transition to turbulence," J. Fluid Mech. **247**, 275 (1993).
[48]B. Vreman, B. Geurts, and H. Kuerten, "Large-eddy simulation of the turbulent mixing layer," J. Fluid Mech. **339**, 357 (1997).
[49]P. Moin, W. Squires, W. H. Cabot, and S. Lee, "A dynamic subgrid-scale model for compressible turbulence and scalar transport," Phys. Fluids A **3**, 2746 (1991).
[50]A. W. Vreman, N. D. Sandham, and K. H. Luo, "Compressible mixing layer growth rate and turbulence characteristics," J. Fluid Mech. **320**, 235 (1996).
[51]U. Piomelli, W. H. Cabot, P. Moin, and S. Lee, "Subgrid-scale backscatter in turbulent and transitional flows," Phys. Fluids A **3**, 1766 (1991).
[52]C. Meneveau, T. S. Lund, and W. H. Cabot, "A Lagrangian dynamic subgrid-scale model of turbulence," J. Fluid Mech. **319**, 353 (1996).
[53]S. Ghosal, T. S. Lund, P. Moin, and K. Akselvoll, "A dynamic localization model for large-eddy simulation of turbulent flows," J. Fluid Mech. **286**, 229 (1995).
[54]D. C. Wilcox, *Turbulence Modeling for CFD* (DCW, La Cañada, 1993).
[55]F. A. Jaberi, R. S. Miller, F. Mashayek, and P. Givi, "Differential diffusion in binary scalar mixing and reaction," Combust. Flame **109**, 561 (1997).
[56]L. L. Smith, R. W. Dibble, L. Talbot, R. S. Barlow, and C. D. Carter, "Laser Raman scattering measurements of differential molecular diffusion in nonreacting turbulent jets of H_2/CO_2 mixing with air," Phys. Fluids **7**, 1455 (1995).
[57]L. L. Smith, R. W. Dibble, L. Talbot, R. S. Barlow, and C. D. Carter,

"Laser Raman-scattering measurements of differential molecular-diffusion in turbulent nonpremixed jet flames of H_2/CO_2," Combust. Flame **100**, 153 (1995).
[58] A. R. Kerstein, M. A. Cremer, and P. A. McMurtry, "Scaling properties of differential molecular diffusion effects in turbulence," Phys. Fluids **7**, 1999 (1995).
[59] M. B. Long, S. H. Starner, and R. W. Bilger, "Differential diffusion in jets using joint PLIF and Lorenz–Mie imaging," Combust. Sci. Technol. **92**, 209 (1993).
[60] V. Nilsen and G. Kosály, "Differential diffusion in turbulent reacting flows," Combust. Flame **117**, 493 (1999).
[61] P. K. Yeung, S. Xu, and K. R. Sreenivasan, "Schmidt number effects on turbulent transport with uniform mean scalar gradient," Phys. Fluids **14**, 4178 (2002).